Super-Resolution T_1 Estimation: Quantitative High Resolution T_1 Mapping from A Set of Low Resolution T_1-Weighted Images With Different Slice Orientations

Gwendolyn Van Steenkiste,[1]* Dirk H. J. Poot,[2,3] Ben Jeurissen,[1] Arnold J. den Dekker,[1,4] Floris Vanhevel,[5] Paul M. Parizel,[5] and Jan Sijbers[1]

Purpose: Quantitative T_1 mapping is a magnetic resonance imaging technique that estimates the spin-lattice relaxation time of tissues. Even though T_1 mapping has a broad range of potential applications, it is not routinely used in clinical practice as accurate and precise high resolution T_1 mapping requires infeasibly long acquisition times.

Method: To improve the trade-off between the acquisition time, signal-to-noise ratio and spatial resolution, we acquire a set of low resolution T_1-weighted images and directly estimate a high resolution T_1 map by means of super-resolution reconstruction.

Results: Simulation and in vivo experiments show an increased spatial resolution of the T_1 map, while preserving a high signal-to-noise ratio and short scan time. Moreover, the proposed method outperforms conventional estimation in terms of root-mean-square error.

Conclusion: Super resolution T_1 estimation enables resolution enhancement in T_1 mapping with the use of standard (inversion recovery) T_1 acquisition sequences. **Magn Reson Med 77:1818–1830, 2017. © 2016 International Society for Magnetic Resonance in Medicine**

Key words: super-resolution; T_1 mapping; relaxometry; reconstruction

INTRODUCTION

The spin-lattice relaxation time, T_1, is one of the fundamental tissue properties on which clinical magnetic resonance imaging (MRI) contrast is based. As, at a fixed field strength, T_1 is an intrinsic biophysical property of tissues (1,2), it is an important differentiating factor for diseases such as multiple sclerosis (3), epilepsy (4) and dementia (5), and for the characterization of tumors (6–8). Furthermore, T_1 is also used for contrast agent uptake studies, as well as for the measurement of perfusion (9,10) and blood volume (11). In a single clinical T_1-weighted image, the signal strength is not only characterized by the tissue but also by the specific pulse sequence parameters such as the inversion time or the flip angle. As such, the intensity in a T_1-weighted image is not quantitative. The image provides only qualitative information and diagnosis relies on visual interpretation. To allow absolute quantification of T_1, a set of T_1-weighted images with different contrast settings (i.e., sequence parameters) is required. From this set of images, a T_1 value can be estimated for each voxel. Unlike conventional qualitative T_1-weighted imaging, quantitative T_1 mapping allows objective comparison across subjects, protocols, sites, and time (12).

The gold standard T_1 sequence is the inversion recovery (IR) spin echo (SE) sequence (13–16). In this sequence, the longitudinal magnetization is inverted, after which the magnetization is allowed to recover back to its equilibrium state during an inversion time TI. The recovery rate is characterized by the tissue-specific relaxation constant T_1. A set of images, with a well-chosen range of inversion times, can be used to quantitatively estimate a T_1 map. Unfortunately, the acquisition time of the set of T_1-weighted images needed for an accurate and precise T_1 map is not clinically feasible (16).

Most developments in T_1 quantification sequences focus on reducing the acquisition time of the T_1-weighted images either by improving the read-out method of the recovering magnetization (17–22)or by using variable flip angles (VFA) (23–26) to generate T_1 contrast. In faster read-out methods, such as fast/turbo spin echo (FSE/TSE) (21,22,27) or echo planar imaging (EPI) (17,28), multiple k-space lines are acquired after inversion of the longitudinal magnetization. Unfortunately, the radio frequency (RF) pulses used in TSE deposit a high energy, which limits the spatial resolution of the images as specific absorption rate (SAR) limits are easily exceeded (22). Furthermore, EPI images generally suffer from spatial distortions due to off resonance effects.

Alternative T_1 quantification schemes are the Look-Locker (LL) method (18) and its variants (19,20), which reduce the acquisition time by measuring multiple read-outs after each inversion pulse. After inversion, the magnetization is progressively tipped into the transverse plane using a series of small flip angles. Unfortunately, the use of these small flip angles results in a lower

[1]iMinds-Vision Lab, Department of Physics, University of Antwerp, Antwerp, Belgium.
[2]Imaging Science and Technology, Delft University of Technology, 2628 CJ, Delft, The Netherlands.
[3]BIGR (Department of Medical informatics and Radiology), Erasmus Medical Center Rotterdam, Rotterdam, The Netherlands.
[4]Delft Center for Systems and Control, Delft University of Technology, 2628, CD Delft, The Netherlands.
[5]Department of Radiology, University of Antwerp, Antwerp University Hospital, Belgium.
Grant sponsor: Fund for Scientific Research-Flanders; Grant number: G037813N; Grant sponsor: Inter-university Attraction Poles Program (P7/11); Grant sponsor: Research Foundation Flanders (to B. J).
*Correspondence to: Gwendolyn Van Steenkiste, Msc; iMinds-Vision Lab, Department of Physics, University of Antwerp, Universiteitsplein 1, N 1.16, Wilrijk, Antwerpen 2610, Belgium. E-mail: Gwendolyn.VanSteenkiste@uantwerpen.be
Received 30 September 2015; revised 11 April 2016; accepted 11 April 2016
DOI 10.1002/mrm.26262
Published online 1 July 2016 in Wiley Online Library (wileyonlinelibrary.com).

signal-to-noise ratio (SNR) of the acquired images (13,17). Moreover, repeatedly sampling the recovering magnetization hastens its recovery (29). Consequently, the measured longitudinal relaxation time will be shorter than T_1. As the measured relaxation time depends on the flip angles, an accurate knowledge of these flip angles is needed for an accurate T_1 estimation. This makes LL type sequences vulnerable to B1 field inhomogeneities (30,31).

A T_1 map can also be estimated from spoiled gradient-echo images acquired at two different flip angles (23–26,32). These VFA methods are known for their ability to acquire high resolution T_1 maps in a short acquisition time. However, to achieve sufficient accuracy and precision, VFA measurements require a careful selection of pulse sequence parameters as well as the knowledge of the flip angles (33). The actual flip angles might differ from their set values due to B1 field inhomogeneities, making the T_1 estimation prone to errors leading to a loss of accuracy of the estimated T_1 map (31,34,35). In general, the choice of T_1 quantification sequence is about finding the right balance between precision, accuracy and speed.

The acquisition time of IR SE and IR TSE can be shortened by acquiring fewer T_1-weighted images. However, this comes at the expense of decreasing the precision of the T_1 map, while precise T_1 estimation is necessary as the clinically observed differences in T_1 values are typically only within a few percent. Alternatively, the acquisition time can also be shortened by acquiring the T_1-weighted images at a lower spatial resolution. As a bonus, increasing the slice thickness increases the SNR of the T_1-weighted images as the signal strength scales linearly with the imaged volume. However, thicker slices suffer from increased partial volume effects, making it harder to distinguish small anatomical structures.

It has been shown that spatial super-resolution (SR) reconstruction provides a better trade-off between acquisition time, spatial resolution and SNR in structural and diffusion MRI by reconstructing a high resolution image from a set of anisotropic multislice images (36–46). The reconstructed high resolution image benefits from the high SNR of the low resolution images, which are acquired with a high in-plane resolution and a low through-plane resolution, that is, thick slices. The resolution is enhanced by acquiring different, complementary resolution information about the object with each low resolution image. This is ensured by acquiring the low resolution images with a shift in the slice direction (39), at three orthogonal slice orientations (36,37,44) or at rotated slice orientations (41,42,46). In quantitative MRI, SR reconstruction benefits from combining the parameter model with the SR model. This has been shown in diffusion MRI, where the diffusion model was combined with the SR model (37,46), allowing the direct estimation of the desired high resolution quantitative MRI parameters from the low resolution images.

In this article, we propose a new SR method, called super-resolution T_1 (SR-T_1), which combines T_1 estimation with super-resolution to reduce the acquisition time of the T_1-weighted images while providing a precise and accurate high resolution T_1 map. In our approach, a high resolution T_1 map is directly estimated from a set of anisotropic low resolution multislice IR TSE images. Additionally, the proposed method incorporates a model-based motion correction scheme. By means of experiments performed on synthetic and clinical data, we show that a precise and accurate high resolution T_1 map can be estimated out of a set of low resolution T_1-weighted images, of which the acquisition time is shorter than that of a direct high resolution acquisition. An early version of this framework was presented at the Annual Meeting & Exhibition of the ISMRM in 2015 (47).

METHODS

In this section, the proposed SR-T_1 estimation method and its acquisition protocol as well as the experiments are described. The SR-T_1 model is based on a combination of a T_1-weighting model and an SR model. To derive this model, we assume that the low resolution T_1-weighted images are acquired with a multislice IRSE sequence as this is the gold standard quantitative T_1 sequence and the least vulnerable to B1 inhomogeneities (48).

Super-Resolution T_1 Model

Let $\boldsymbol{r}_m \in \mathbb{R}^{N_r \times 1}$ ($m = 1, \ldots, M$, with M the number of images) be a vector representing the $N_{\boldsymbol{r}}$ (unknown) intensities $r_m(j)$ (with j the voxel index, $j = 1, \ldots, N_{\boldsymbol{r}}$) of a noiseless, high resolution T_1-weighted MR image with inversion time TI_m, and sampled at the N_r 3D grid points $\boldsymbol{x} \in \mathbb{R}^{3 \times N_r}$. Furthermore, let $\boldsymbol{s}_m \in \mathbb{R}^{N_s \times 1}$ be a vector of $N_{\boldsymbol{s}}$ signal intensities $s_m(l)$ (with l the voxel index, $l = 1, \ldots, N_{\boldsymbol{s}}$) of a noiseless low resolution T_1-weighted MR image at the same inversion time TI_m and sampled at the N_s 3D grid points $\boldsymbol{y} \in \mathbb{R}^{3 \times N_s}$. Finally, let $\boldsymbol{A}_m = (a_m(l,j)) \in \mathbb{R}^{N_s \times N_r}$ be a linear operator defining the transformation of the high resolution image $\boldsymbol{r}_m$ to the low resolution image $\boldsymbol{s}_m$. Then, the signal magnitude in voxel l of $\boldsymbol{s}_m$ may be described as:

$$s_m(l) = \left| \sum_{j=1}^{N_r} a_m(l,j) r_m(j) \right|, \qquad [1]$$

Introducing the homogeneous coordinates $\boldsymbol{x}'(j) = (\boldsymbol{x}^T(j)\,1)^T$ and $\boldsymbol{y}'(l) = (\boldsymbol{y}^T(l)\,1)^T$, the elements of the projection matrix $\boldsymbol{A}_m$ can be described as

$$a_m(l,j) = \omega(\boldsymbol{U}_m(\boldsymbol{M}_m \boldsymbol{x}'(j)) - \boldsymbol{y}'(l)), \qquad [2]$$

with $\boldsymbol{U}_m \in \mathbb{R}^{4 \times 4}$ an (augmented) affine transformation matrix that maps the points in the high resolution space, $(\boldsymbol{x}(j))$, to the points in the low resolution space, $(\boldsymbol{y}(l))$, $\boldsymbol{M}_m \in \mathbb{R}^{4 \times 4}$ an (augmented) affine transformation matrix describing motion, and ω a point spread function (PSF). The PSF ω is defined by the MR image acquisition method. For multislice acquisition methods that sample a rectangular part of the k-space, ω can be modeled as the product of three 1D PSFs that are applied in the three orthogonal directions aligned with the MR image coordinate axes. The PSFs in the frequency and phase encoding direction are defined by the rectangular part of the k-space that is regularly sampled and can thus be

modeled by Dirichlet, or periodic sinc, functions. The through-plane PSF depends on the slice selection method. Slice selection is often performed by applying either a (windowed) sinc or a Gaussian shaped RF pulse, so the sampling in the through-plane (i.e., slice) direction can be modeled by a (smoothed) box or a Gaussian function, respectively (42). In this work, a windowed sinc RF pulse was used, so the slice excitation profile was modeled by a smoothed box function.

If the repetition time TR $\gg T_1$, the (unknown) intensities of the high resolution T_1-weighted image $\boldsymbol{r}_m$ can be written in function of the spin-lattice relaxation time $T_1(j)$, with $\boldsymbol{T}_1 \in \mathbb{R}^{N_r \times 1}$, and a quantity $\rho(j)$, with $\boldsymbol{\rho} \in \mathbb{R}^{N_r \times 1}$, which is proportional to the proton density (48):

$$r_m(j) = \rho(j)\left(1 - (1 - \cos\theta)e^{-\frac{\mathrm{TI}_m}{T_1(j)}}\right), \quad [3]$$

with θ the inversion angle and TI_m the inversion time at which r_m is acquired.

By combining Eqs. [1] and [3], the magnitude of the low resolution T_1-weighted image, $\boldsymbol{s}_m$, can be described in terms of a high resolution T_1 and ρ map:

$$s_m(l; \boldsymbol{T}_1, \boldsymbol{\rho}) = \left|\sum_{j=1}^{N_r} a_m(l,j)\rho(j)\left(1 - (1 - \cos\theta)e^{-\frac{\mathrm{TI}_m}{T_1(j)}}\right)\right|. \quad [4]$$

The acquired low resolution images $\tilde{\boldsymbol{s}}_m \in \mathbb{R}^{N_s \times 1}$ are subject to noise. When a single coil MR acquisition system is considered, the noisy voxel intensities $\tilde{s}_m(l)$ can be modeled as Rician distributed random variables (49,50). For a multicoil acquisition, the data are governed by a non-central chi distribution (49,51). When the SNR is high enough ($\gg 3$), which is typically the case for the low resolution voxels $\tilde{s}_m(l)$, both distributions are well approximated by a Gaussian distribution (50–52). Therefore, in this work we adopt the assumption of Gaussian distributed noise.

Super-Resolution T_1 Estimation

By combining all low resolution images, a high resolution ρ and T_1 map can be estimated by minimizing the squared difference between the acquired low resolution T_1-weighted images $\tilde{\boldsymbol{s}}_m$ and the low resolution T_1-weighted images generated by the model (Eq. [4]):

$$\hat{\boldsymbol{T}}_1, \hat{\boldsymbol{\rho}} = \arg\min_{\boldsymbol{T}_1, \boldsymbol{\rho}} \left\{\sum_{m=1}^{M}\sum_{l=1}^{N_s} ||\tilde{s}_m(l) - s_m(l; \boldsymbol{T}_1, \boldsymbol{\rho})||_2^2\right\}, \quad [5]$$

where the choice of the least squares criterion is motivated by the Gaussian noise assumption. However, this nonlinear least squares (NLS) problem is typically ill-conditioned in the sense that its solution is very sensitive to noise. To make the solution more stable and less noisy, regularization terms that penalize large variations in the estimated ρ and T_1 map are included, leading to the following regularized NLS estimator:

$$\hat{\boldsymbol{T}}_1, \hat{\boldsymbol{\rho}} = \arg\min_{\boldsymbol{T}_1, \boldsymbol{\rho}} \left\{\sum_{m=1}^{M}\sum_{l=1}^{N_s} ||\tilde{s}_m(l) - s_m(l; \boldsymbol{T}_1, \boldsymbol{\rho})||_2^2 + \lambda_1||\Delta\boldsymbol{T}_1||_2^2 + \lambda_2||\Delta\boldsymbol{\rho}||_2^2\right\}, \quad [6]$$

with Δ the 3D discrete Laplace operator, and λ_1 and λ_2 the corresponding weighting factors (41,46).

Implementation

In the in vivo experiments described in the Experiments section, the transformation $\boldsymbol{U}_m$ (Eq. [2]) was formed by combining the transformation matrix provided by the DICOM header information retrieved from the scanner and a world to voxel transformation. The transformation $\boldsymbol{U}_m$ was combined with the transformation $\boldsymbol{M}_m$ into a single affine transformation, which was applied efficiently using a combination of shear transformations as described by Poot et al. (42). The parameters constituting the motion operator $\boldsymbol{M}_m$ were estimated by an iterative model-based motion correction scheme (53,54). During the first step of this iterative scheme, $\boldsymbol{M}_m$ was the identity matrix. First, each acquired low resolution image was upsampled to the high resolution grid with the adjoint operator $\boldsymbol{A}'_m$. Next, a T_1 and ρ map were estimated from these upsampled images by NLS fitting the modulus of the model in Eq. [3] to the data with the Levenberg-Marquardt algorithm. From these maps, low resolution images were simulated using Eq. [4]. Finally, these simulated images were rigidly aligned to the acquired images based on mean squared differences minimization, which in turn updates $\boldsymbol{M}_m$. All steps were repeated until the relative decrease in the cost function was smaller than 10^{-6}. The motion operator $\boldsymbol{M}_m$ as well as the T_1 and ρ map that resulted from this procedure were then used to initialize the SR-T_1 estimation.

For both the in vivo and simulation experiments, the regularization parameter λ_2 was chosen aiming at equal contributions of $\lambda_1||\Delta\boldsymbol{T}_1||_2^2$ and $\lambda_2||\Delta\boldsymbol{\rho}||_2^2$ to the penalty. To do so, $||\Delta\boldsymbol{T}_1||_2^2$ and $||\Delta\boldsymbol{\rho}||_2^2$ were calculated from the initial estimates of the T_1 and ρ map. The ratio between those two values is then the ratio between λ_2 and λ_1. As such, only one regularization weight, λ_1, remains, which was chosen by experimenting with a range of values and qualitatively (i.e., visually) determining the best result. The values of λ_1 and λ_2 were then kept constant during the reconstruction. The cost function was minimized with a trust-region Newton method (55).

The algorithm was implemented using Matlab (MATLAB2014a, The Mathworks Inc.m, Natick, USA) on a PC with a hexa-core CPU @ 3.20 GHz with 64 GB of RAM. The in vivo experiment described in the Experiments section required around 19 GB RAM and the running time was 4.58 hours.

Acquisition Protocol

In MRI, there is a consensus that resolution enhancement is not achievable in the in-plane directions, as the Fourier encoding scheme excludes aliasing in the frequency and phase encoding directions (56). Therefore,

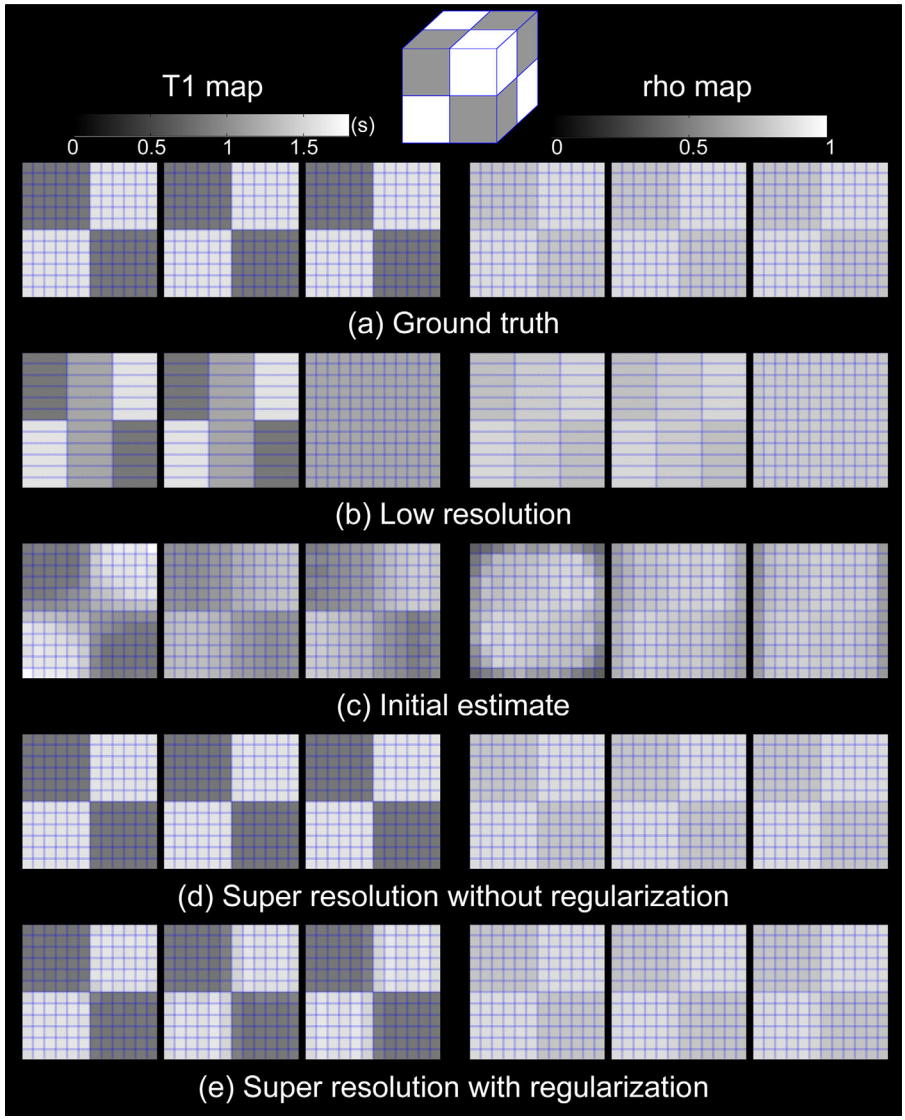

FIG. 1. 3D view of the numerical phantom and three orthogonal views of the (**a**) ground truth (**b**) low resolution, (**c**) initial estimate, (**d**) SR ($\lambda_1 = \lambda_2 = 0$), (**e**) SR ($\lambda_1 = 1.0 \cdot 10^{-3}$ and $\lambda_2 = 1.9 \cdot 10^{-4}$) T_1 map (left) and ρ map (right). The blue lines depict the borders of the voxels.

the low resolution T_1-weighted images are acquired with an isotropic in-plane resolution and a slice thickness larger than this in-plane resolution. In multislice acquisitions, increasing the slice thickness improves the SNR of the acquired images. Moreover, as less slices need to be acquired to cover the region of interest (ROI), the acquisition time will be reduced. Throughout this work, the anisotropy of the voxels is quantified with an anisotropy factor α, defined as the ratio between the slice thickness and the voxel size in the frequency encoding and phase encoding direction.

To recover the high resolution information, the low resolution images need to contain complementary information about the object. Rotation in image space results in a rotation in frequency domain. As such, acquiring the low resolution images with different slice orientations ensures that each low resolution image covers a different part of k-space. As argued by Plenge et al. (40), this results in a more effective sampling of k-space than by shifting the low resolution images by subpixel distances along the slice selection direction. In the latter case, the narrow slice selection frequency band covers the same part of the k-space for each low resolution image, making the SR reconstruction rely heavily on recovering the aliased high frequency in the slice encoding direction. While the proposed reconstruction method does not imply restrictions on the acquisition setup and the slice orientations, we chose to rotate the slice orientations around the phase encoding axis over sub-pixel shifts in the slice encoding direction. By rotating the slice orientation around the phase encoding axis, each low resolution image has the same phase encoding direction. This assures that image artefacts, that might occur in the phase encoding direction, such as blurring due to a higher T_2-weighing of the signal, will be the same for each low resolution image, and thus will not introduce misalignment between the low resolution images. The number of slice orientations, n, was chosen as:

$$n = \left[\frac{\pi}{2}\alpha\right], \qquad [7]$$

with the operator $[\cdot]$ denoting that n is rounded to the closest natural number. By acquiring n images, rotated

Table 1
Overview of the Slice Orientations and Corresponding Inversion Times TI_m.

Orientation	TI_m (ms)
S	100
	624
$S > T$ 25.7°	370
	2310
$T > S$−38.6°	220
	1370
$T > S$−12.9°	130
	811
$T > S$ 13.0°	480
	3000
$T > S$ 38.6°	284
	1780
$S > T$−25.7°	169
	1050

T = transversal and S = sagittal

around the phase encoding axis in incremental steps of $180°/n$, the k-space of the high resolution imaged object will be filled with a minimal overlap and thus a minimal number of slice orientations (40,46).

Experiments

The quality of the high resolution T_1 and ρ maps estimated with the proposed SR-T_1 method was evaluated with both synthetic and in vivo data sets. To improve the numerical performance of the fitting algorithms, the signal intensities of the simulated and in vivo data sets were scaled so that the range of the estimated ρ map equals that of the T_1 map (57).

Numerical Simulations

The proposed SR-T_1 estimator was first evaluated on a simple numerical phantom (Fig. 1a). The $12 \times 12 \times 12$ phantom consisted of distinct regions that are characterized by one out of two T_1 values, corresponding to the T_1 of gray matter (1.607 s) and white matter (0.838 s) (58). From this phantom, which served as ground truth, two noiseless low resolution data sets, with size $12 \times 12 \times 3$ were simulated. The first data set consisted of fourteen T_1-weighted images, each simulated with a unique inversion time, $TI \in [0.1, \ldots, 3s]$ and all TI equidistant in log space. An overview of the inversion times can be found in Table 1. The second data set consisted of seven subsets, each simulated with a different slice orientation and each containing two T_1-weighted images. Each of the in total fourteen T_1-weighted images had a unique inversion time, which were equal to the ones used in the first data set. From the first data set, a low resolution T_1 map with size $12 \times 12 \times 3$, was estimated using a voxel-wise T_1 estimation. From the second data set, a high resolution T_1 map with size $12 \times 12 \times 12$, was estimated twice using SR-T_1: once without regularization ($\lambda_1 = \lambda_2 = 0$ in Eq. [6]) to show that the parameters are identifiable and once with regularization, $\lambda_1 = 1.0 \cdot 10^{-3}$ and $\lambda_2 = 1.9 \cdot 10^{-4}$ to assess the smoothing caused by the regularization.

Whole Brain Simulations

Noiseless $434 \times 362 \times 362$ T_1 and ρ maps were generated by combining an anatomical model of a normal human brain (59) with T_1 and ρ values measured in human brain tissue at 3T (58,60). For the three main tissues the used T_1 values were: 0.838 s for white matter, 1.607 s for gray matter and 4.3 s for cerebrospinal fluid (CSF). The ρ map was normalized with the maximum value of ρ such that $\rho_j \in [0, \ldots, 1]$. From these maps, 50 T_1-weighted images, with size $120 \times 120 \times 120$, were simulated each with a different TI, where the TIs were selected in the interval $[0.1, \ldots, 15]$s, equidistantly spaced in the log space. Next, from these T_1-weighted images a $120 \times 120 \times 120$ T_1 and ρ map were estimated by voxel-wise NLS fitting using the model in Eq. [3]. These maps served as the ground truth maps from which two low resolution T_1-weighted data sets, with noise standard deviation 0.02 and size $120 \times 120 \times 30$, were simulated using Eq. [1]. The SNR, defined as the ratio of the spatial mean to the standard deviation of the signal, was calculated in a small homogeneous white matter region in a T_1-weighted image simulated with TI = 100 ms and found to be equal to 115. Both data sets were composed of 14 T_1-weighted images, each simulated with a unique inversion time, equidistant in the log space. An overview of the inversion times can be found in Table 1. In the first data set, LR1, all low resolution T_1-weighted images were simulated with the same slice orientation. As such, this data set corresponds to a conventional T_1-weighted data set with a low, anisotropic resolution. The second data set, LR2, was simulated according to the proposed SR acquisition setup. This data set consisted of seven subdata sets, each containing two T_1-weighted images. Each subset was simulated with a different slice orientation by rotating about the phase encoding axis in incremental steps of 25.7°.

Both data sets were simulated 50 times, each time with a different noise realization. From each LR1 data set, a $120 \times 120 \times 120$ T_1 map was estimated by transforming the low resolution T_1-weighted images to the $120 \times 120 \times 120$ high resolution grid with the adjoint operator $\boldsymbol{A}\prime$ prior to applying the conventional voxel-wise T_1 estimation method. From each LR2 data set, a $120 \times 120 \times 120$ T_1 map was estimated using the proposed SR-T_1 estimation method with $\lambda_1 = 50$ and $\lambda_2 = 1.32$.

In Vivo Data

To evaluate the proposed SR-T_1 method with human in vivo data, several T_1-weighted data sets of a healthy 28-year old male volunteer were acquired with a Prismafit (3T; Siemens AG, Siemens Medical Solution, Erlangen, Germany) using a 32-channel head coil. To limit the scan time per session, the data sets were acquired during three different scan sessions. One data set was acquired with VFA, the other data sets were acquired with an interleaved multislice IR TSE, with turbo factor 10, without slice gap and with 100% sampling. Each IR TSE data set was acquired at fourteen different inversion times, which were the same as those used in the simulation experiments (Table 1). The slice thickness of the

Table 2
Overview of the Relevant Acquisition Parameters of the Clinical Data Sets.

Data set	In-plane resolution (mm^2)	Slice thickness (mm)	Acquisition matrix	Slices	Brain coverage (%)	n	M	TR (ms)	TE (ms)	Scan time (min)
LR1	1×1	4	256×256	40	100	1	14	5000	8.8	28
LR2	1×1	4	256×256	40	100	7	14	5000	8.8	28
LR2a	1×1	4	256×256	40	100	7	14	5000	8.8	28
LR2b	1×1	4	256×256	40	100	7	14	5000	8.8	28
VFA	1×1	1	256×256	144	100	1	–	10	2.0	7
HR	1×1	1	256×256	40	28	1	14	6000	11	30

n is the number of slice orientations and M the number of inversion times.

anisotropic low resolution data set was chosen to have whole brain coverage without exceeding SAR limits. A detailed overview of the acquisition parameters of these data sets can be found in Table 2. During the first scan session the following data sets were acquired:

- **LR1**: $1 \times 1 \times 4\,mm^3$ IR TSE data set. All fourteen T_1-weighted images were acquired with the same slice orientation.
- **LR2**: $1 \times 1 \times 4\,mm^3$ IR TSE data set consisting of seven subsets, each including two T_1-weighted images. Each subset had a different slice orientation, which was rotated around the phase encoding direction in incremental steps of 25.7°. The slice orientations are given in Table 1. Each of the in total 14 low resolution T_1-weighted images was acquired at a different inversion time (Table 1).
- **VFA**: $1 \times 1 \times 1\,mm^3$ VFA data set consisting of two T_1-weighted images acquired with the flip angle set to 4° and 21°.

During the second scan session the following data sets were acquired:

- **LR2a** and **LR2b**: Two data sets were acquired with the same acquisition setup as the one used for the **LR2** data set from the first scan session.

During the third scan session the following data set was acquired:

- **HR**: $1 \times 1 \times 1\,mm^3$ IR TSE T_1-weighted data set. To limit acquisition time and SAR deposit, only 40 slices were acquired in the sagittal direction.

From the LR1 data set, a T_1 and ρ map were estimated with the following conventional T_1 estimation procedure. First, the acquired images were corrected for motion by rigid registration using mutual information. Next, the corrected images were upsampled to a $1 \times 1 \times 1\,mm^3$ grid with the adjoint operator $\boldsymbol{A}\prime$. Finally, a $1 \times 1 \times 1\,mm^3$ T_1 and ρ map were estimated using a voxel-wise NLS fit optimized with the Levenberg-Marquardt algorithm. The same procedure, without the upsampling, was used to estimate a $1 \times 1 \times 1\,mm^3$ T_1 and ρ map from the HR data set. The proposed SR-T_1 method ($\lambda_1 = 1.0 \cdot 10^{-3}, \lambda_2 = 0.6 \cdot 10^{-3}$) was used to estimate $1 \times 1 \times 1\,mm^3$ T_1 and ρ maps from the data sets LR2, LR2a, and LR2b. From the VFA data set, a $1 \times 1 \times 1\,mm^3$ T_1 map was calculated using a voxel-wise LS fit (25).

The T_1 and ρ maps estimated from the different data sets were compared qualitatively by visual inspection. Furthermore, the spatial resolution of the different T_1 maps was assessed by measuring the average width over 25 edge profiles. The edge width, defined as the width (in high resolution voxels) from 10% to 90% of the edge height, was measured by least squares fitting of the sigmoid function (39):

$$f(q) = a_1 + \frac{a_2}{1 + \exp\left(-a_3(q - a_4)\right)}, \qquad [8]$$

where it is easy to show that the edge width is given by $4.4/a_3$. The SNR of the T_1-weighted data sets was computed in a uniform region in the corpus callosum of the T_1-weighted image acquired with TI = 100 ms. For the data set VFA, the SNR was computed in the image acquired with flip angle set to 21°. Additionally, to assess the precision of the T_1 estimation, the standard deviation of the estimated T_1 maps was computed in a uniform region in the corpus callosum.

RESULTS

Numerical Simulations

Figure 1 shows the ground truth phantom, three orthogonal views of the ground truth T_1 and ρ map (Fig. 1a) and the T_1 and ρ map for the different estimation methods. In the low resolution, T_1 and ρ map (Fig. 1b) the partial volume effects are so large that in the middle slice the structure of the phantom is not visible. In the initial estimated T_1 map (Fig. 1c), the structure of the phantom is visible in the middle slices. However, the edges between the different tissues are blurred. In the corresponding ρ map, the structures are not visible. Using SR-T_1 clearly enhances the spatial resolution of the estimated T_1 and ρ map (Fig. 1d,e): they both approximate the ground truth very well. In the reconstruction without regularization (Fig. 1d), the edges between the two different tissues are sharp. Although the use of regularization (Fig. 1e) does result in a minor smoothness of the edges between the tissues, it is clear that SR-T_1 still outperforms the initial estimation and the low resolution estimation.

Synthetic Whole Brain Simulations

In Figure 2, an orthogonal view of the T_1 and ρ maps estimated from the GT data, the LR1 data and the LR2 data are shown. The respective root-mean-square error (RMSE) maps are shown in the second row. In Table 3 the RMSE, absolute bias and standard deviation averaged over the white matter voxels (WM) and the gray matter

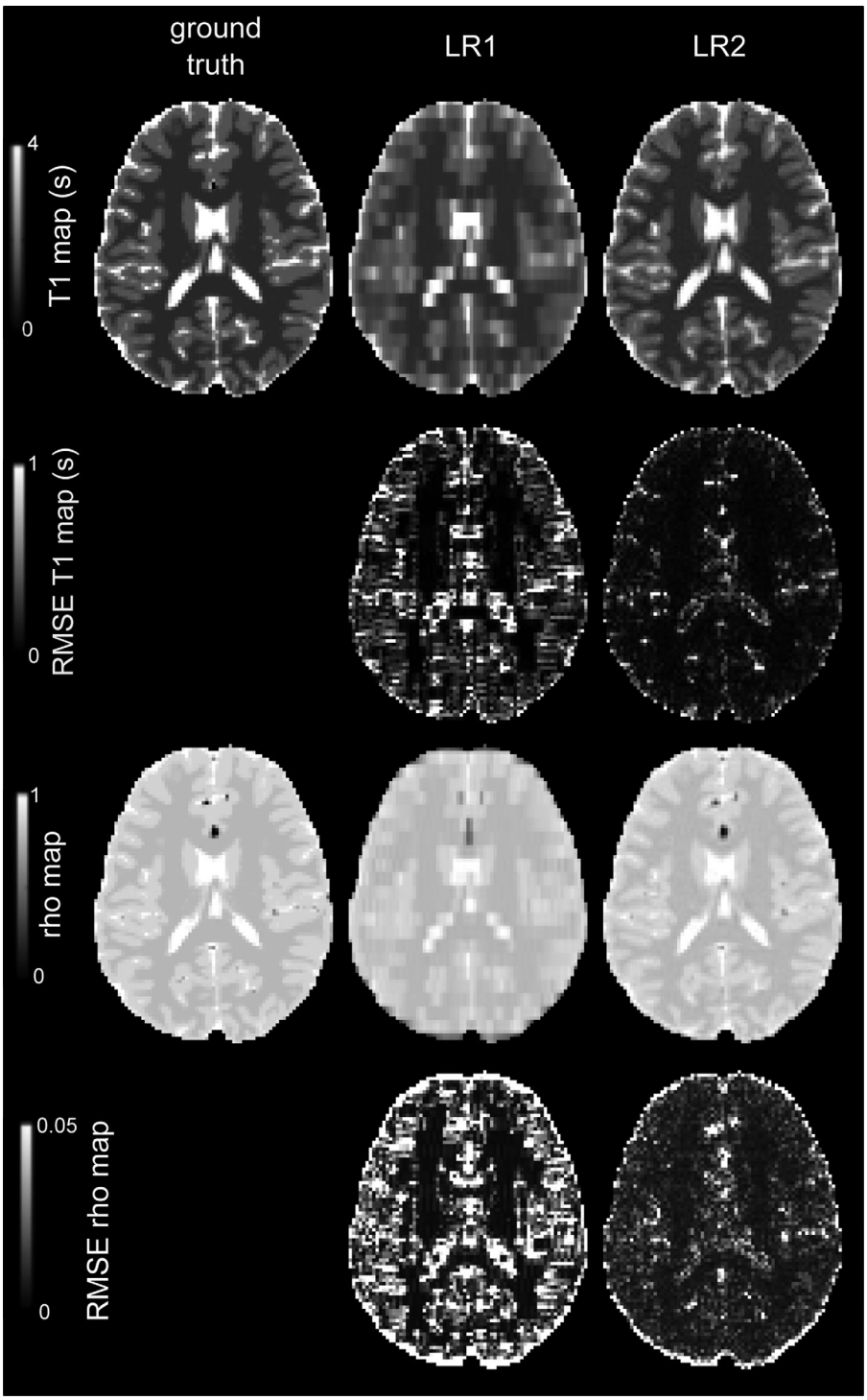

FIG. 2. Transversal slice of the T_1, RMSE T_1, ρ and RMSE ρ maps from the conventional T_1 estimation on LR1 and the SR-T_1 estimation on LR2.

voxels (GM) are given. The voxel-wise estimated T_1 and ρ maps (LR1 in Fig. 2) suffer from high partial volume effects due to the low spatial resolution of the T_1-weighted images. The SR-T_1 estimation enhances the resolution of the T_1-weighted images from data set LR2. In the resulting T_1 and ρ map (super resolution in Fig. 2), fine structures are clearly visible, while in the voxel-wise estimated T_1 and ρ map the fine structures are blurred. This is supported by the RMSE: overall the RMSE is smaller for the T_1 and ρ map estimated with SR-T_1 than for the voxel-wise estimated T_1 and ρ map. Although the standard deviation is higher for the SR-T_1 estimation than for the voxel-wise estimation, the bias is much lower.

In Vivo Data

In Table 4 the SNR of the acquired data sets is given. As the low resolution data sets (LR1, LR2, LR2a, and LR2b)

Table 3
RMSE, Bias and Standard Deviation (std) of the T_1 and ρ Estimator Averaged Over the White Matter (WM) and Gray Matter (GM) Voxels.

	WM LR1	WM LR2	GM LR1	GM LR2
RMSE $\hat{T}_1$ (s)	0.119	0.040	0.203	0.097
Bias $\hat{T}_1$ (s)	0.119	0.036	0.203	0.092
Std $\hat{T}_1$ (s)	0.003	0.015	0.002	0.021
RMSE $\hat{\rho}$	0.010	0.008	0.029	0.014
Bias $\hat{\rho}$	0.009	0.005	0.028	0.012
Std $\hat{\rho}$	0.002	0.005	0.002	0.005

are acquired with the same spatial resolution, their SNR should be the same. Additionally, Table 4 also reports the spatial mean, standard deviation and SNR (defined as the ratio of the spatial mean to the standard deviation) calculated in a uniform region of the corresponding estimated T_1 map. There is a small loss in precision for the SR-T_1 estimation method compared with the conventional voxel-wise NLS estimation from T_1-weighted images with a low spatial resolution. Note, however, that as the low resolution data had a different acquisition time than the high resolution data, no direct comparison can be made between the standard deviations and SNR of the different T_1 maps. However, taking into account that the standard deviation is inversely proportional to the square root of the scan time, and that only 28% of the brain was covered within 30 minutes of scan time, it is clear that the standard deviation of the estimated HR T_1 map would be almost four times as low as the one given in Table 4 when the whole brain would have been acquired within 30 minutes.

Figure 3 shows a transversal and coronal slice of the ρ and T_1 map estimated from the data set LR1 and from the data set LR2. Due to the low spatial resolution of the T_1-weighted images, many partial volume effects occur in the conventional voxel-wise estimated T_1 (Fig. 3a) and ρ (Fig. 3c) map from data set LR1, blurring fine structures. Estimating the T_1 (Fig. 3b) and ρ (Fig. 3e) map with SR-T_1 enhances the spatial resolution of the T_1 and ρ map, reducing the partial volume effects. As a result, the interfaces between the different tissue types are more clear. This can be appreciated even more from the zooms shown in Figure 3. A transversal zoom on the caudate nucleus-head, the putamen and the globus pallidus is shown. In the zoom on the T_1 and ρ map estimated from the data set LR1, the three different structures are hard to distinguish from each other. In the T_1 and ρ map estimated with SR-T_1 from the data set LR2, the interface between the different tissue types is more clear, making it easier to outline the different structures. The same can be seen in the coronal zoom on the cerebellum. The interface between white and gray matter is better defined for the SR T_1 map than for the LR1 T_1 map. This is confirmed by the edge width measurement. The average edge width for the data set LR1 is 5.3 voxels and for data set LR2 2.1 voxels.

In Figure 4, a sagittal slice from the T_1 map estimated with SR-T_1 from the data set LR2a (Fig. 4b) is compared with one from the T_1 map which was voxel-wise estimated from the data set HR (Fig. 4a). In both slices, the same level of fine structures can be observed. This is supported by the edge width which is 2.1 voxels for the data set HR. Moreover, visually, both T_1 maps show a similar range of T_1 values. This is supported by the average T_1 value in a homogeneous region in the corpus callosum which is given in Table 4.

Figure 5 shows three orthogonal views of the T_1 maps estimated using SR-T_1 from the data set LR2a (Fig. 5a) and the data set LR2b (Fig. 5b). Visually, both T_1 maps exhibit the same level of details. In Figure 5, the average and standard deviation of the T_1 values within three homogeneous regions (one in each tissue type), is reported. It is clear that both T_1 maps show a similar range of T_1 values in the different tissues.

Figure 6 shows three orthogonal slices of the T_1 map estimated from the VFA data set and of the T_1 map estimated with SR-T_1 from the LR2 data set. Although the VFA data set is acquired at an isotropic $1 \times 1 \times 1\text{mm}^3$ resolution, small structures cannot be distinguished properly due to the noise and image artefacts.

DISCUSSION

Increasing the spatial resolution in quantitative T_1 mapping is challenging because of the trade-off between the spatial resolution, the acquisition time, and the SNR. To improve this trade-off, we proposed a new SR acquisition and reconstruction method specific for quantitative T_1 mapping, SR-T_1. The reconstruction method combines SR reconstruction and T_1 estimation into one integrated approach, enabling the direct estimation of an isotropic high resolution T_1 map from a set of anisotropic low

Table 4
For Each Data Set (Column 1), the SNR of the Acquired T_1-Weighted Data (Column 2), the Applied Estimation Method (Column 3), the Spatial Average (Column 4) and Standard Deviation (Column 5) of T_1 in a Uniform Region of the Corpus Callosum in the Corresponding Estimated T_1 Maps, Are Given

Data set	SNR acquired data	Estimation method	Average T_1 (ms)	Std T_1 (ms)	SNR T_1
LR1	15.75	voxel-wise NLS	476	23.86	19.95
LR2	15.75	SR-T_1	475	32.10	14.80
LR2a	14.91	SR-T_1	483	33.00	14.64
LR2b	15.01	SR-T_1	477	34.33	13.90
VFA	24.98	voxel-wise NLS	1040	94.22	11.04
HR	5.30	voxel-wise NLS	487	35.94	13.55

Column 6 gives the SNR of the T_1 maps, which is calculated by dividing the average T_1 by the std of the T_1 estimator. Note that only the data sets starting with 'LR' have the same acquisition time. As the acquisition times of the VFA and HR data set are different, the standard deviations of these T_1 maps cannot be compared directly.

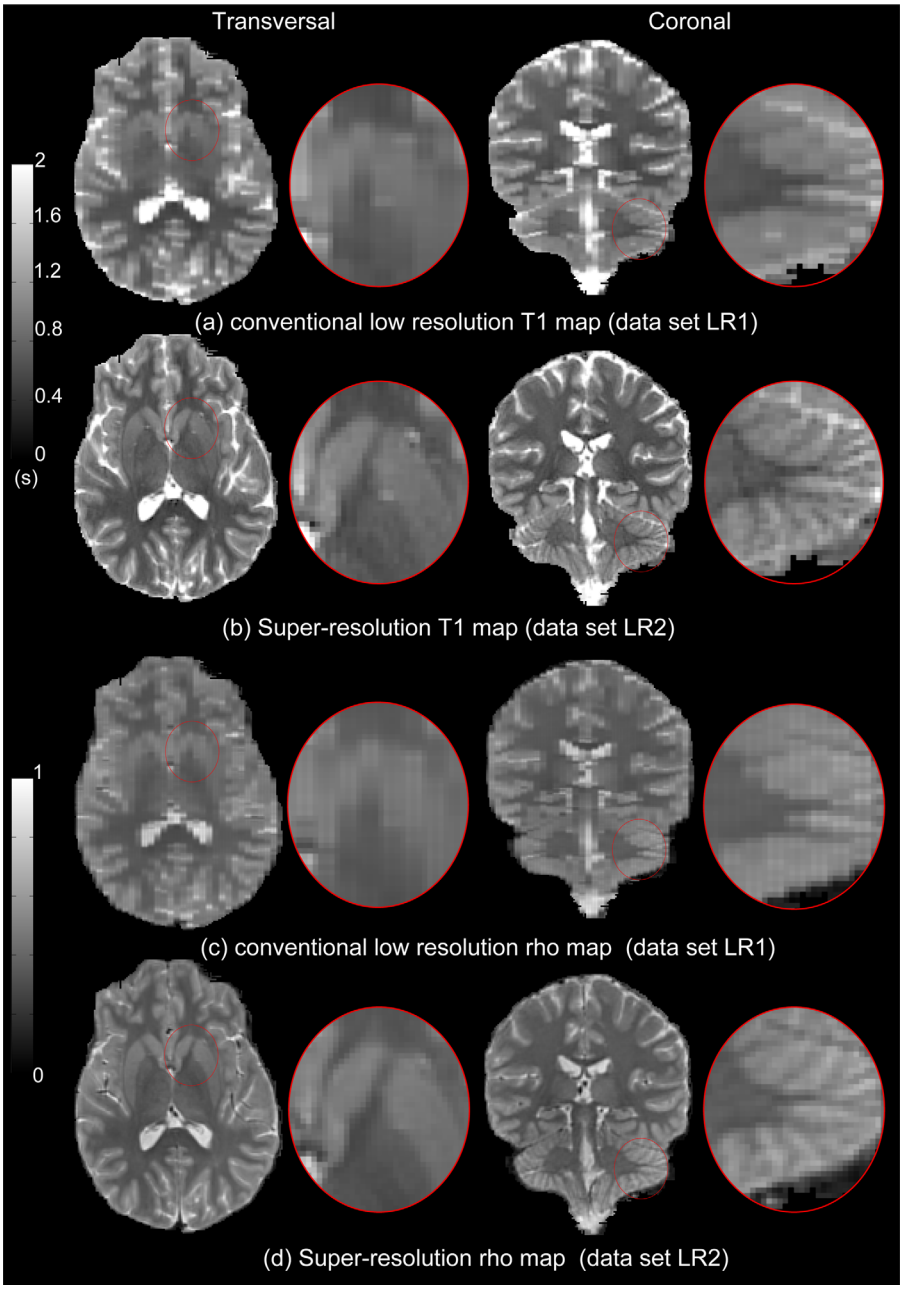

FIG. 3. Transversal and coronal view and zoom in of the T_1 maps and ρ maps estimated from (**a**, **c**) data set LR1 and (**b**, **d**) data set LR2.

resolution T_1-weighted images. A direct acquisition of a set of high resolution T_1-weighted images needed for whole brain T_1 mapping is infeasible due to the SAR limitations. By increasing the slice thickness and thus decreasing the number of slices needed for whole brain coverage, the energy deposited by the pulses decreases. As such, by acquiring anisotropic low resolution T_1-weighted images, the SAR limit is not exceeded.

Using simple numerical simulations we have shown that the specific acquisition scheme and iterative reconstruction can recover high resolution information. These results are confirmed by the whole brain simulation, where the T_1 maps estimated from two low resolution data sets are compared with the ground truth T_1 map. Both low resolution data sets have the same acquisition time as they have the same resolution and number of inversion time. They differ only in the acquisition geometry as one of the data sets is simulated with different slice orientations. The results show that the SR-T_1 method enhances the resolution and improves the RMSE of the T_1 and ρ estimator, compared with a conventional voxel-wise T_1 estimation. The simulation experiment also shows an increase in the standard deviation when SR-T_1 mapping is used over conventional voxel-wise T_1 estimation. By increasing the regularization strength (λ_1, λ_2) the standard deviation will decrease (increase of precision), however, this comes at the cost of an increased bias and blurring of the fine structures. This same trend is observed in the in vivo experiment. Both visual comparison with a conventional low and high resolution data set as well as the computation of the average edge width, show that SR-T_1 improves the spatial resolution of the acquired low resolution T_1-weighted

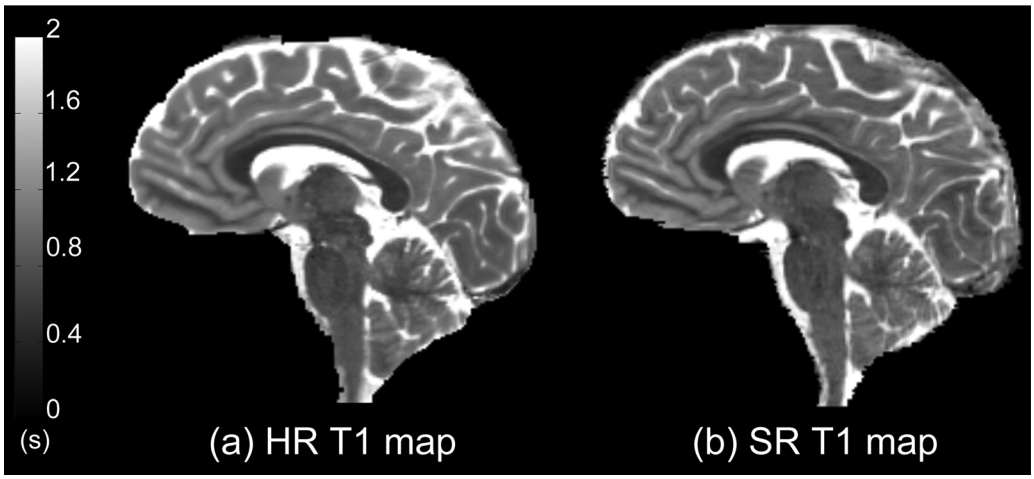

FIG. 4. Sagittal slice of (**a**) the HR T_1 map and (**b**) the SR-T_1 T_1 map estimated from data set LR2b.

images. The in vivo experiments also show that multiple experiments with the same setup, result in similar T_1 maps, showing that the proposed SR-T_1 method provides reproducible results.

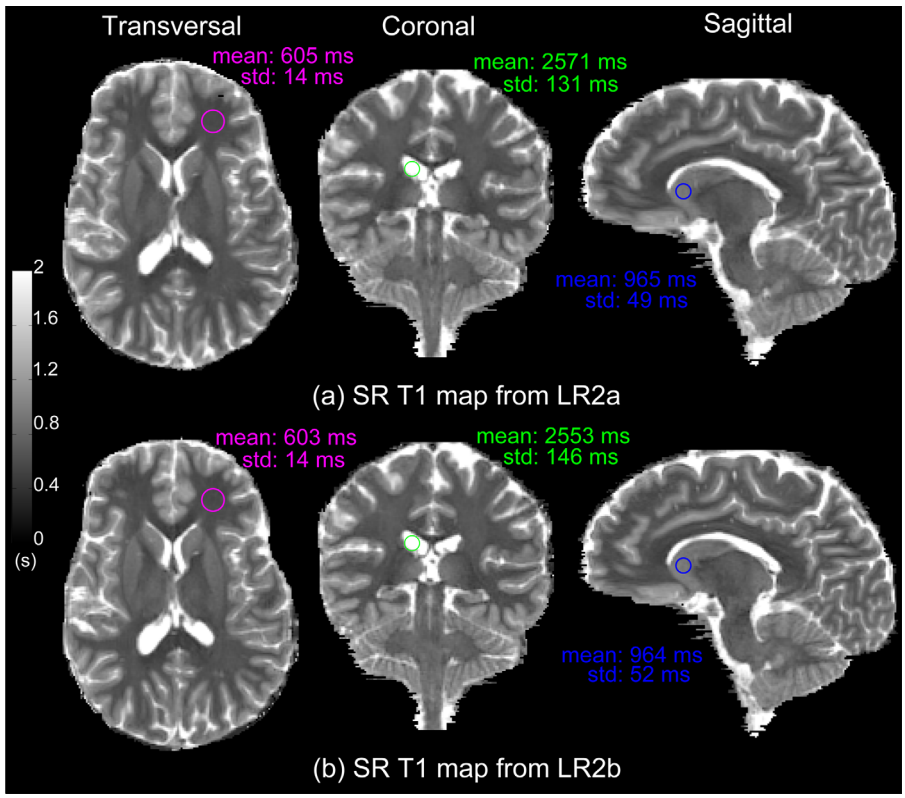

FIG. 5. Transversal, coronal and sagittal slice of the SR-T_1 T_1 map estimated from (**a**) data set LR2a and (**b**) data set LR2b. Mean and standard deviation values of T_1 are calculated in the areas marked by the differently colored circles. The pink circle lies in the white matter, the green circle in the CSF and the blue circle in de caudate nucleus.

In this article, we demonstrated that SR-T_1 can improve the resolution while maintaining the same acquisition time and SNR of the acquired images. Alternatively, the proposed SR-T_1 technique can also be used to shorten the acquisition time or to improve the SNR of the estimated T_1 maps. Improving the acquisition time would enable quantitative T_1 mapping in clinical routine. As the anisotropic T_1-weighted images are acquired with less slices, their acquisition time will be shorter. If the same number of inversion times is used as for the isotropic T_1-weighted images, the overall acquisition time decreases. The isotropic resolution information is then recovered by the iterative reconstruction. By improving the SNR of the acquired images, the precision of the T_1 estimator increases. Because of their thick slices, the anisotropic low resolution T_1-weighted images have a higher SNR than isotropic high resolution T_1-weighted images. Furthermore, as the acquisition time of the low resolution T_1-weighted images is shorter, more inversion times can be acquired within the same overall acquisition time than when high resolution T_1-weighted images are used.

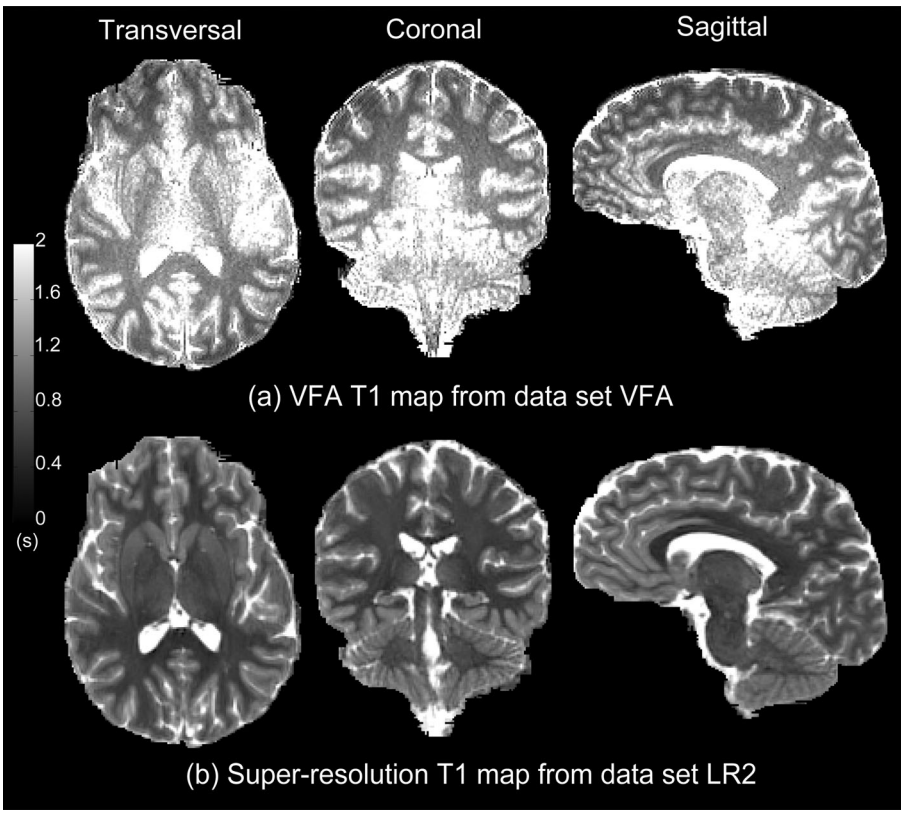

FIG. 6. Transversal, coronal and sagittal slice of (**a**) the T_1 map estimated from data set VFA and (**b**) the SR-T_1 T_1 map estimated from data set LR2.

For both the conventional NLS estimator and the proposed SR-T_1 estimator, the T_1 values estimated from the data acquired with the IR TSE sequence are lower than those estimated from the VFA data and those found in literature (58,61,62). Note, however, that the T_1 values reported in literature are quite diverse and depend on the acquisition settings such as echo train length and the number of acquired slices (58,63). Possible reasons for the underestimation of T_1 are magnetization transfer effects, interslice cross-talk, inversion profile effects, short TR, perfusion effects (22,31,63,64). However, the factors leading to the different in vivo T_1 relaxation times still have to be thoroughly investigated. Our simulations show that the SR-T_1 estimator is accurate and precise. Moreover, comparing a T_1 map estimated with SR-T_1 with a T_1 map estimated with a conventional technique (upsampling followed by voxelwise fitting), shows that comparable T_1 values are found. Thus the bias is not caused by the proposed SR-T_1 estimator but by the incapability of the signal model to describe the signal accurately. As suggested by Zhu et al. (22), this bias can be significantly reduced by a correction scheme based on linear regression which calculates the "true" T_1 from the underestimated T_1, which, however, is outside the scope of this work.

In the in vivo experiments, we chose to combine the proposed SR-T_1 with the widely available IR TSE sequence. However, the proposed method can also be combined with faster T_1 sequences, such as IR TSE with time-efficient slice ordering (22) or simultaneous multislice techniques (65), which would shorten the acquisition time.

CONCLUSION

In this article, we proposed SR-T_1, a new T_1 estimation method which combines SR reconstruction with T_1 parameter estimation into one integrated estimation method and produces a high resolution T_1 map directly from a set of low resolution T_1-weighted images. Furthermore, a specific acquisition scheme for these low resolution T_1-weighted images, using a stock sequence, was provided. The proposed technique enables high resolution $1 \times 1 \times 1\text{mm}^3$ whole-brain IR T_1 mapping, previously infeasible with IR due to SAR limitations. As the technique is complementary with other acquisition schemes, faster T_1 sequences could be combined with SR-T_1, which would enable the use of quantitative high resolution T_1 mapping through SR-T_1 in clinical routine.

ACKNOWLEDGMENT

The authors would like to thank Steven Baete for his valuable input on the acquisition settings.

REFERENCES

1. Bottomley PA, Hardy CJ, Argersinger RE, Allen-Moore G. A review of 1H nuclear magnetic resonance relaxation in pathology: are T1 and T2 diagnostic? Med Phys 1987;14:1–37.
2. Oros-Peusquens AM, Laurila M, Shah NJ. Magnetic field dependence of the distribution of NMR relaxation times in the living human brain. Magn Reson Mater Phys 2008;21:131–147.
3. Truyen L, van Waesberghe JHTM, van Walderveen MAA, van Oosten BW, Polman CH, Hommes OR, Adèr HJA, Barkhof F. Accumulation of hypointense lesions ("black holes") on T1 spin-echo MRI correlates with disease progression in multiple sclerosis. Neurology 1996;47:1469–1476.
4. Conlon P, Trimble M, Rogers D, Callicott C. Magnetic resonance imaging in epilepsy: a controlled study. Epilepsy Res 1988;2:37–43.

5. Erkinjuntti T, Ketonen L, Sulkava R, Vuorialho M, Livanainen M. Do white matter changes on MRI and CT differentiate vascular dementia from Alzheimer's disease? J Neurol Neurosurg Psychiatry 1987;50:37–42.
6. Englund E, Brun A, Györffy-Wagner Z, Larsson E-M, Persson B. Relaxation times in relation to grade of malignancy and tissue necrosis in astrocytic gliomas. Magn Reson Imaging 1986;4:425–429.
7. Kurki T, Komu M. Spin-lattice relaxation and magnetization transfer in intracranial tumors in vivo: effects of Gd-DTPA on relaxation parameters. Magn Reson Imaging 1995;13:379–385.
8. Naruse S, Horikawa Y, Tanaka C, Hirakawa K, Nishikawa H, Yoshizaki K. Significance of proton relaxation time measurement in brain edema, cerebral infarction and brain tumors. Magn Reson Imaging 1986;4:293–304.
9. Kershaw LE, Buckley DL. Precision in measurements of perfusion and microvascular permeability with T1-weighted dynamic contrast-enhanced MRI. Magn Reson Med 2006;56:986–992.
10. Peeters F, Annet L, Hermoye L, Van Beers BE. Inflow correction of hepatic perfusion measurements using T1-weighted, fast gradient-echo, contrast-enhanced MRI. Magn Reson Med 2004;51:710–717.
11. Cheng HLM. T1 measurement of flowing blood and arterial input function determination for quantitative 3D T1-weighted DCE-MRI. J Magn Reson Imaging 2007;25:1073–1078.
12. Ashton E. Quantitative MR in multi-center clinical trials. J Magn Reson Imaging 2010;31:279–288.
13. Crawley AP, Henkelman RM. A comparison of one-shot and recovery methods in T1 imaging. Magn Reson Med 1988;7:23–34.
14. Drain LE. A direct method of measuring nuclear spin-lattice relaxation times. Proc Phys Soc Lond A 1949;62:301–306.
15. Hahn EL. An accurate nuclear magnetic resonance method for measuring spin-lattice relaxation times. Phys Rev 1949;76:145–146.
16. Tofts P. Quantitative MRI of the brain. Hoboken, NJ: Wiley; 2003.
17. Clare S, Jezzard P. Rapid T1 mapping using multislice echo planar imaging. Magn Reson Med 2001;45:630–634.
18. Look DC, Locker RR. Time saving in measurement of NMR and EPR relaxation times. Rev Sci Instrum 1970;41:250–251.
19. Messroghli DR, Buehrer M, Kozerke S, Nordmeyer S, Dietrich T, Atrott K, Hucko T, Paetsch I, Berger F, Fleck E. Simultaneous T1 mapping, cine imaging, and IR-prepared imaging of the rat heart using Small Animal Look-Locker Inversion recovery (SALLI). In Proceedings of the 18th Annual Meeting of ISMRM, Stockholm, Sweden, 2010. Abstract 490.
20. Messroghli DR, Rudolph A, Abdel-Aty H, Wassmuth R, Kühne T, Dietz R, Schulz-Menger J. An open-source software tool for the generation of relaxation time maps in magnetic resonance imaging. BMC Med Imaging 2010b;16:1–8.
21. Mulkern RV, Wong ST, Winalski C, Jolesz FA. Contrast manipulation and artifact assessment of 2D and 3D RARE sequences. Magn Reson Imaging 1990;8:557–566.
22. Zhu DC, Penn RD. Full-brain T1 mapping through inversion recovery fast spin echo imaging with time-efficient slice ordering. Magn Reson Med 2005;54:725–731.
23. Deoni SCL. High-resolution T1 mapping of the brain at 3T with driven equilibrium single pulse observation of T1 with high-speed incorporation of RF field inhomogeneities (DESPOT1-HIFI). J Magn Reson Imaging 2007;26:1106–1111.
24. Deoni SCL. Quantitative relaxometry of the brain. Top Magn Reson Imaging 2010;21:101–113.
25. Deoni SCL, Peters TM, Rutt BK. High-resolution T1 and T2 mapping of the brain in a clinically acceptable time with DESPOT1 and DESPOT2. Magn Reson Med 2005;53:237–241.
26. Trzasko JD, Mostardi PM, Riederer SJ, Manduca A. Estimating T1 from multichannel variable flip angle SPGR sequences. Magn Reson Med 2013;69:1787–1794.
27. Mansfield P. Multi-planar image formation using NMR spin echoes. J Phys C Solid State 1977;10:55–58.
28. Mansfield P. Real-time echo-planar imaging by NMR. Br Med Bull 1984;40:187–190.
29. Kay I, Henkelman RM. Practical implementation and optimization of one-shot T1 imaging. Magn Reson Med 1991;22:414–424.
30. Kaptein R, Dijkstra K, Tarr CE. A single-scan Fourier transform method for measuring spin-lattice relaxation times. J Magn Reson Imaging 1976;24:295–300.
31. Stikov N, Boudreau M, Levesque IR, Tardif CL, Barral JK, Pike GB. On the accuracy of T1 mapping: searching for common ground. Magn Reson Med 2015;73:514–522.
32. Liberman G, Louzoun Y, Ben Bashat D. T1 mapping using variable flip angle SPGR data with flip angle correction. J Magn Reson Imaging 2014;40:171–180.
33. Preibisch C, Deichmann R. Influence of RF spoiling on the stability and accuracy of T1 mapping based on spoiled FLASH with varying flip angles. Magn Reson Med 2009;61:125–135.
34. Liu Y, Buck JR, Zheng S, Ikonomidou VN. Optimizing and comparing the efficiencies of relaxometry sequences in quantitative T1 and T2 imaging. In Proc Intl Soc Mag Reson Med, Toronto, Ontario, Canada; Vol. 23, 2015. p. 1689.
35. Mintzopoulos D, Inati S. The effects of magnetic field inhomogeneity on FLASH-based T1 measurements. In Proc Intl Soc Mag Reson Med, Seattle, Washington, USA; Vol. 14, 2006. p. 923.
36. Fogtmann M, Seshamani S, Kim K, Chapman T, Studholme C. A unified approach for motion estimation and super resolution reconstruction from structural magnetic resonance imaging on moving subjects. In MICCAI Workshop on Perinatal and Paediatric Imaging, Nice, France; 2012. pp. 9–26.
37. Fogtmann M, Seshamani S, Kroenke C, Cheng X, Chapman T, Wilm J, Rousseau F, Studholme C. A unified approach to diffusion direction sensitive slice registration and 3-D DTI reconstruction from moving fetal brain anatomy. IEEE Trans Med Imaging 2014;33:272–289.
38. Greenspan H. Super-resolution in medical imaging. Comput J 2009; 52:43–63.
39. Greenspan H, Oz G, Kiryati N, Peled S. MRI inter-slice reconstruction using super-resolution. Magn Reson Imaging 2002;20:437–446.
40. Plenge E, Poot DHJ, Bernsen M, Kotek G, Houston G, Wielopolski P, Van Der Weerd L, Niessen WJ, Meijering E. Super-resolution methods in MRI: can they improve the trade-off between resolution, signal-to-noise ratio, and acquisition time? Magn Reson Med 2012;68:1983–1993.
41. Poot DHJ, Jeurissen B, Bastiaensen Y, Veraart J, Van Hecke W, Parizel PM, Sijbers J. Super-resolution for multislice diffusion tensor imaging. Magn Reson Med 2013;69:103–113.
42. Poot DHJ, Van Meir V, Sijbers J. General and efficient super-resolution method for multi-slice MRI. In: Lect Notes Comput Sc, Beijing: Springer, Berlin, Heidelberg; Vol. 6361, 2010. pp. 615–622.
43. Robinson MD, Chiu SJ, Toth CA, Izatt JA, Lo JY. Novel applications of super-resolution in medical imaging. In: Milanfar, P, editor. Super-Resolution Imaging. Boca Raton: CRC Press; 2010. pp. 383–412.
44. Scherrer B, Gholipour A, Warfield SK. Super-resolution reconstruction to increase the spatial resolution of diffusion weighted images from orthogonal anisotropic acquisitions. Med Image Anal 2012;16: 1465–1476.
45. Van Reeth E, Tham IW, Tan CH, Poh CL. Super-resolution in magnetic resonance imaging: a review. Concept Magnetic Reson 2012; 40A:306–325.
46. Van Steenkiste G, Jeurissen B, Veraart J, den Dekker AJ, Parizel PM, Poot DHJ, Sijbers J. Super-resolution reconstruction of diffusion parameters from diffusion-weighted images with different slice orientations. Magn Reson Med 2016;75:181–195.
47. Van Steenkiste G, Poot DHJ, Jeurissen B, den Dekker AJ, Sijbers J. Super-resolution T1 mapping: a simulation study. In Proc Intl Soc Mag Reson Med, 2015. p. 1679.
48. Bernstein MA, King KF, Zou XJ. Handbook of MRI pulse sequences. London: Elsevier Academic press; 2004.
49. den Dekker AJ, Sijbers J. Data distributions in magnetic resonance images: a review. Phys Med 2014;30:725–741.
50. Gudbjartsson H, Patz S. The Rician distribution of noisy MRI data. Magn Reson Med 1995;34:910–914.
51. Constantinides CD, Atalar E, McVeigh ER. Signal-to-noise measurements in magnitude images from NMR phased arrays. Magn Reson Med 1997;38:852–857.
52. Andersen AH, Kirsch JE. Analysis of noise in phase contrast MR imaging. Med Phys 1996;23:857–869.
53. Bai Y, Alexander DC. Model-based registration to correct for motion between acquisitions in diffusion MR imaging. In IEEE International Symposium on Biomedical Imaging, Paris, France; 2008, 5. pp. 947–950.
54. Ramos-Llordén G, den Dekker AJ, Van Steenkiste G, Van Audekerke J, Verhoye M, Sijbers J. Simultaneous motion correction and T1 estimation in quantitative T1 mapping: an ML restoration approach. In IEEE International Conference on Image Processing (ICIP), Quebec City, Canada, 2015. pp. 3160–3164.
55. Coleman TF, Li Y. On the convergence of interior-reflective Newton methods for nonlinear minimization subject to bounds. Math Program 1994;67:189–224.

56. Scheffler K. Superresolution in MRI? Magn Reson Med 2002;47:392–397.
57. Gill PE, Murray W, Wright MH. Practical optimization. London: Academic Press; 1981.
58. Wright PJ, Mougin OE, Totman JJ, et al. Water proton T1 measurements in brain tissue at 7, 3, and 1.5 T using IR-EPI, IR-TSE, and MPRAGE: results and optimization. Magn Reson Mater Phys 2008;21:121–130.
59. Cocosco CA, Kollokian V, Kwan RKS, Evans AC. BrainWeb: online interface to a 3D MRI simulated brain database. Neuroimage 1997;5:S425.
60. Gold GE, Suh B, Sawyer-Glover A, Beaulieu C. Musculoskeletal MRI at 3.0 T: initial clinical experience. Am J Roentgenol 2004;183:343–351.
61. Badve C, Yu A, Rogers M, Ma D, Liu Y, Schluchter M, Sunshine J, Griswold M, Gulani V. Simultaneous T1 and T2 brain relaxometry in asymptomatic volunteers using magnetic resonance fingerprinting. Tomography 2015;1:136–144.
62. Wansapura JP, Holland SK, Dunn RS, Ball WS, Jr. NMR relaxation times in the human brain at 3.0 tesla. J Magn Reson Imaging 1999;9:531–538.
63. Eldeniz C, Finsterbusch J, Lin W, An H. TOWERS: T-One with enhanced robustness and speed. Magn Reson Med 2016;76:118–126.
64. van Gelderen P, Jian X, Duyn J. Effects of magnetization transfer on T1 contrast in human brain white matter. Neuroimage 2016;128:85–95.
65. Gagoski BA, Bilgic B, Eichner C, Bhat H, Grant PE, Wald LL, Setsompop K. RARE/turbo spin echo imaging with simultaneous multislice wave-CAIPI. Magn Reson Med 2015;73:929–938.